Expansion Mass Spectrometry Imaging: Achieving One-Micron Level Resolution for Lipid Analysis in Tissues

Yik Ling Winnie Hung [a], Chengyi Xie [a,b], Jianing Wang [a]*, Xin Diao [a,b], Xiaoxiao Wang [a,b], Shulan Qiu[c], Jiacheng Fang [a], Zongwei Cai [a,b]*

[a] State Key Laboratory of Environmental and Biological Analysis, Hong Kong Baptist University, Hong Kong SAR, China

[b] Department of Chemistry, Hong Kong Baptist University, Hong Kong SAR, China

[c] Department of Health Technology and Informatics, The Hong Kong Polytechnic University (PolyU), Hong Kong SAR, China

* Corresponding Authors:

Dr. Jianing Wang, Email: j_wang@hkbu.edu.hk

Prof. Zongwei Cai, Email: zwcai@hkbu.edu.hk

Abstract

A novel physical method for enhanced resolution, termed expansion mass spectrometry imaging (Ex-MSI), has been developed for lipid mass spectrometry imaging, utilizing existing commercially available mass spectrometers without necessitating modifications. This approach involves embedding tissue sections in a swellable polyelectrolyte gel, with the target biomolecules indirectly anchored to the gel network. By employing matrix-assisted laser desorption ionization mass spectrometry imaging (MALDI-MSI), the method has realized an enhancement in spatial resolution that surpasses the conventional resolution limits of commercial instruments by approximately 4.5 folds. This allows for the detailed visualization of fine structures in the mouse brain, testis, and liver. The method achieves a subcellular level resolution (less than 2.5 μm) across various tissues and attains a lateral spatial resolution approaching 1 μm. As a physical technique for achieving resolution beyond standard capabilities, this approach is readily adaptable and presents a powerful tool for high-definition imaging in biological research.

Introduction

In recent decades, the need for high spatial resolution imaging has grown significantly across various disciplines in biological research[1-3]. This technology has become a pivotal tool in not only identifying chemical components within cells and tissues but also elucidating intricate cellular structures, functions, and interactions. In the context of disease, high spatial resolution imaging is invaluable for detecting biomarkers, thus playing a crucial role in the prevention, diagnosis, treatment, and monitoring of various conditions. Beyond biomedicine, it also fosters progress in fundamental research, aiding in the understanding of biological processes at the molecular and subcellular levels. Such insights are integral to discoveries in fields ranging from cell biology to neuroscience[4].

One common approach to achieve molecular high spatial resolution imaging is confocal or super-resolution fluorescence microscopy. However, this method has certain limitations[5, 6]. It relies on fluorescent dyes, which emit over a broad range of wavelengths, leading to signal interference. Additionally, the need to use multiple dyes to investigate different species within one experiment can complicate the process. Fluorescence microscopy-based methods are effective means of presenting the spatial localization of proteins. However, methods based on optical fluorescence imaging lack the means to image small molecules with high molecular specificity.

Mass spectrometry imaging (MSI) has emerged to address these challenges[7-9]. MSI offers the advantage of being label-free, enabling the direct detection of numerous chemical species in a single experiment. This includes the ability to analyze both large biomolecules, such as proteins and peptides, and smaller biomolecules, like lipids and metabolites. Unlike fluorescence microscopy, MSI does not rely on complex labeling processes or the use of exogenous dyes. This simplifies the procedure, making it a more versatile and effective method for studying

cellular structures and functions. Secondary Ion Mass Spectrometry (SIMS) has been used to achieve high spatial resolution, even down to 200 nm. However, SIMS has its problems, including a tendency for the ions to break apart, which reduces sensitivity[10]. Other methods, such as multiplexed ion beam imaging (MIBI) and imaging mass cytometry (IMC)[11-15], have their own unique features but also have limitations, such as the need for costly tags and limits on what can be detected simultaneously. Furthermore, MIBI and IMC are specific methods aimed at spatial proteomics and are not suitable for analyzing metabolites and lipids.

Matrix-assisted laser desorption ionization mass spectrometry imaging (MALDI-MSI) has emerged as a promising method in the pursuit of high spatial resolution molecular imaging[10, 16-27]. This technique has the distinct advantage of retaining various intact biomolecules without the need for labeling, making it particularly appealing for studying complex biological structures. Among the available soft ionization techniques, MALDI-MSI offers the highest spatial resolution, with commercial settings typically achieving around 5-µm resolution. Innovations in methods such as scanning microprobe MALDI (SMALDI) have managed to push this limit even further, reaching resolutions as fine as 1.4-µm[16]. Transmission mode optics have led to even more significant advancements, with some experiments achieving an impressive 0.6-µm resolution[18]. However, these remarkable achievements often come with challenges. They may require customized instrumentation, sophisticated optics design, and intricate sample preparation. These complexities can hinder the broad adoption of these methods, posing obstacles to their widespread commercialization.

In response to these challenges, we have developed Expansion Mass Spectrometry Imaging (Ex-MSI), an innovative method that increases the spatial resolution of MALDI-MSI to the subcellular level without the need for modifications in laser optics. Inspired by expansion microscopy[28-39], Ex-MSI physically expands the tissue slice embedded in an expandable hydrogel, achieving a 4.5-fold increase in spatial resolution without relying on the mass

spectrometer itself. This unique approach does not necessitate a new matrix deposition method and can be readily adopted across different instruments. In this work, we demonstrate the effectiveness of lipid Ex-MSI across mouse organs with diverse structural properties at subcellular level resolution. We reveal the method's capability to delineate fine and compact structures at a 1-µm resolution level. The Ex-MSI method holds significant promise for the broader application of high lateral spatial resolution MALDI-MSI in biological and clinical disciplines, potentially accelerating medical research and drug development in the near future.

Results and Discussion

Development of Ex-MSI Workflow

Physical expansion for ultra-high-resolution mass spectrometry imaging requires several key conditions: effective expansion of the sample, retention of the molecules to be measured and their effective ionization. In this study, we adopted gelation formulations used in expansion microscopy (ExM)[28, 29, 34, 36-39]. The experimental details are described in the supplemental information. Fig. 1 shows the schematic workflow of Ex-MSI. Fresh mouse brain was first fixed. Anchor molecule (AcX) was then linked to the proteins in tissue slices. Unlike ExM, where the tissue slice could freely flow in the gelation solution, the tissue slice for MSI must be laid flat and stuck evenly to the bottom of the gelation chamber. During gelation, proteins were anchored to the gel network and lipids could be retained through electrostatic interactions between proteins and lipids in mild conditions. The compact tissue structures were destroyed in digestion for even expansion. The hydrogel was then dried on the ITO slide. To achieve high spatial resolution MSI, fine matrix droplets were deposited onto the hydrogel using pneumatic-assisted electrospray deposition. The mass spectrometry imaging parameter was optimized to enhance the signal-to-noise ratio lipid peaks. After MS acquisition, the data was analyzed by SCiLS Lab software.

After building the basic framework of the Ex-MSI workflow, the expansion factor and uniformity were determined. Concerning the expansion method, Suppl. Fig. 1a presents the mouse brain hippocampus region embedded in the gel before expansion, where the bottom width was 4.5 mm. After expansion, the bottom width became 26 mm (Suppl. Fig 1b) and it remained 23mm after drying (Suppl. Fig. 1c). The expansion factor could reach up to 5 folds (~4.5 folds on average). In Suppl. Fig. 1d, the optical image obtained by bright-field microscopy and the MSI image exhibited on the left and right, respectively. The relative

position and the shapes of the critical features in both images resemble each other. On the other hand, we performed MALDI-MSI for consecutive tissue slices to ascertain expansion uniformity. The MSI images of m/z 419.2 could show the outline of the tissue (Suppl. Fig. 1e). We separately performed without (left image) and with (right image) tissue expansion MSI for two adjacent tissue sections. The overlapped stacking comparison in Suppl. Fig. 1f showed that there was no obvious distortion in the shape of the tissue slices after overlaying the two MSI images together. We could confirm that our Ex-MSI method could uniformly expand and dehydrate tissue.

To further improve the method, some critical steps were optimized. In ExMSI experiments, tissue thickness is a factor that influences the spectrum quality, like peak intensity and signal-to-noise ratio. Suppl. Fig. 2a shows the signal intensity comparison of lipid Ex-MSI using 30, 40, and 50-µm tissue sections. Representative lipids, five phosphatidylcholines (PC) and five sphingomyelins (SM) were selected as listed in Suppl. Table 1 and their signal intensities in ten random ROIs across the coronal cerebrum tissue section were averaged. Among the ten lipids, 50-µm slices generally provided the highest signal intensities. As the tissue thickness increased from 30 to 50 µm the signal intensities mostly doubled. Suppl. Fig. 2b presents the representative mass spectra of the three experimental conditions. In addition to the increase in signal intensity, more lipid peaks could also be detected. For example, $[M+K]^+$ of SM (d38:1) was only detected in 50-µm slice. Thus, 50-µm slices would be used in the following experiments. On the other hand, the gel is sometimes fractured after drying. To prevent this, the drying process should also be well controlled to prevent gel fracturing. Thus, instead of putting the gel into a desiccator directly for overnight dehydration, we engineered a custom dark box equipped with controls to regulate the drying conditions of the hydrogel.

In MALDI-MSI, the selection of matrix is one of the dominant factors to the molecules ionized from the tissue sample, and hence the sensitivity of different groups of lipids. 1,5-

Diaminonaphthalene (1,5-DAN), 9-aminoacridine (9AA) and N-(1-Naphthyl) Ethylenediamine Dihydrochloride (NEDC) are commonly used matrices for analysis of lipids[22, 23, 40-47]. Suppl. Fig. 2c displays the average mass spectra obtained from mouse brain tissue after expansion imaged at 50 µm acquisition resolution. Only a background matrix signal could be obtained using 1,5-DAN. The main reason is that this matrix tends to fragment and form multimers at higher laser energies. Comparing lipid diversity of Ex-MSI using 9AA and NEDC, the detection of lipids using 9AA mainly focused on m/z 850 – 950 region and the signal of sulfatide (ST), SHexCer (42:2;O2) at m/z 888.6 dominated the mass spectra. Using NEDC matrix, apart from sulfatide, phosphatidylethanolamine (PE), phosphatidylinositol (PI) and phosphatidylserine (PS) of low signal intensity were found. Based on our own experience and known reports, NEDC exhibits very high sensitivity and a wide detection range for metabolites and lipids in the negative ion mode. Consequently, NEDC was selected as the matrix in the Ex-MSI negative mode analysis.

When the dried gel sample with matrix deposited was observed under a microscope, it was found that the tissue was exposed and laid flat on the ITO slide instead of being embedded and curved in gel, which usually occurs in ordinary expansion microscopy conditions. Surface flatness was critical to MSI experiments, especially under high spatial resolution imaging, and our method was capable of such application. To investigate the effect on imaging quality improvement after expansion, we imaged mouse brain regions using different spatial resolutions and the results were compared in Fig. 2. By increasing the laser rastering acquisition resolution from 50 to 5 µm, which was equivalent to the imaging resolution of 11 to 1.1 µm, the Ex-MSI shows significantly improved image resolution.

Ex-MSI of lipids in mouse brain

We first demonstrated Ex-MSI of lipids in mouse brain under positive and negative mode, respectively. To illustrate the effect of Ex-MSI, samples with and without expansion were prepared using consecutive coronal brain slices. The caudoputamen (CP) of the striatum region was imaged with 50 and 20 µm spatial resolution under positive mode with 2,5-Dihydroxybenzoic acid (DHB) as a matrix. In Fig. 2a, the ion images of m/z 850.8, $[M+Na]^+$ ion of PC (O-36:4) were shown. The characteristic fibrous morphology of CP could hardly be observed without expansion (left) at 50 µm acquisition resolution. With ExMSI (right), the morphology could be seen even at 50-µm acquisition resolution with 4.5-fold expansion (equivalent to 11-µm spatial resolution). For comparative purposes, we directly imaged a slice of mouse brain cerebrum using a 10-µm laser raster spot. The resulting ion images, presented in Fig. 2b, were of comparable quality, thereby validating the strength of our methodology. When the CP was subjected to imaging at an acquisition resolution of 20 µm with expansion, translating to an equivalent image resolution of 4.4 µm, intricate structural details were clearly unveiled, as illustrated in Fig. 2c. The CP was additionally imaged using 20 and 10 µm acquisition resolutions in negative ion mode, employing NEDC as the matrix. Ion images corresponding to m/z 888.6, representing the $[M-H]^-$ ion of SHexCer (42:2;O2), achieved an equivalent resolution of 4.4 µm, as shown in Fig. 2d (right) and further reached a resolution of 2.2 µm as shown in Fig. 2e (right). This achievement gains added significance when considering that the 5-µm acquisition resolution is the upper limit of currently commercially available instruments. Under these circumstances, ensuring stable data acquisition becomes a formidable challenge, and the quality of matrix deposition must meet rigorous standards. Nevertheless, by employing a more readily attainable 10-µm acquisition resolution, Ex-MSI allows for imaging capabilities that exceed the inherent resolution boundaries of the equipment. Moreover, this enhancement in resolution is independent of the instrument's inherent

capabilities, offering the potential for further improvement as the equipment's resolution evolves.

We further conducted comparative studies at the instrument's limit of 5-µm resolution. After upgrading the microGRID system, our instrument is now capable of high-precision 5-µm data acquisition. We performed 5-µm acquisition on a localized region of the CP after expansion, achieving an equivalent resolution of 1.1 µm. The magnified image of the same region at an equivalent 4.4-µm resolution is shown on the left panel in Fig. 2f. It is indicated that our expansion mass spectrometry imaging (Ex-MSI) is compatible with 5-µm acquisition criteria, leading to further enhancement in resolution. Fig. 2g presents mass spectrometry imaging of a localized area at the junction between the hippocampus and cortex, demonstrating the method's capability to break through the 5-µm resolution limit and further reveal intricate details at an equivalent 1.1-µm resolution. Even with the extensive dilution of lipids due to the multi-fold expansion of the sample, a broad range of lipids could still be efficiently detected (Suppl. Fig 3). This highlights that Ex-MSI is a robust tool for molecular imaging, offering both sensitivity and high resolution.

To further demonstrate Ex-MSI's capability in capturing both complex morphology and intricate chemical compositions in brain tissue, we imaged a large region of a coronal brain slice at a 10-µm acquisition resolution in negative ion mode. Fig. 3b showcases an overlaid ion image at an equivalent 2.2-µm resolution for several lipid species including PE (38:4) ($[M-H]^-$, m/z 766.5), PE (40:6) ($[M-H]^-$, m/z 790.5), and SHexCer (40:1;O2) ($[M-H]^-$, m/z 862.6) via Ex-MSI, revealing their distinct distribution patterns within the brain. Figs. 3c-e provides enlarged ion images for various lipid classes, comparing the 2.2-µm equivalent resolution obtained through expansion (right or bottom) against the 10-µm native resolution (left or top). The regions of interest for these images are highlighted in Fig. 3b. Notably, the fibrous structure in the dorsal part of the lateral geniculate complex becomes apparent only when imaged using

Ex-MSI (Fig. 3c). In Figs. 3d and 3e, the ion images display the distribution of PA (40:6) ([M-H]$^-$, m/z 747.5) and SHexCer (42:2;O2) ([M-H]$^-$, m/z 888.6) in the ventral posteromedial nucleus of the thalamus, highlighting the region's complex and compact structure enriched with diverse lipid species.

Despite the dilution and loss of lipids caused by sample expansion, we still achieved the detection of multiple species of lipids, and the decrease in detectable species was not too much lower than that of non-expanded samples. Suppl. Fig. 4 displays the mass spectra of mouse brain tissues after expansion under positive and negative modes, respectively. There are 74 and 167 endogenous species that were found in positive and negative mode, respectively. Amongst, 125 of them were assigned as lipids with mass error within 5 ppm for positive and negative mode, respectively. The peak list with corresponding lipid assignments can be found in Suppl. Table 2 and 3. To sum up, 19 lipid classes were detected. In positive mode, PC dominated, while in negative mode, PE contributed the most. Suppl. Table 4 shows the list of CID fragments from selected lipids and their identities under positive and negative mode, respectively.

Compared to light microscopy, which typically necessitates intricate labeling and staining for specific chemical visualization, mass spectrometry imaging (MSI) offers the unique capacity to capture a broad spectrum of chemical compounds in one analytical session. Importantly, MSI is particularly adept at the accurate identification and imaging of small molecules, a task that is often challenging in traditional light microscopy. Ex-MSI augments these capabilities by achieving exceptional spatial resolution without compromising chemical specificity. Therefore, Ex-MSI serves as a superior method for obtaining both high-resolution images and a wealth of chemical information, particularly for small molecular species.

Ex-MSI of lipids in mouse testis

In addition to applications in mouse brain, Ex-MSI was employed to analyze mouse testicular tissue. Sulfogalactosylglycerolipid (SGG) is pivotal to male fertility due to their essential role in spermatogenesis. Furthermore, their spatial distribution could serve as an indicator of seminoma. Sections of mouse testes were prepared both with and without tissue expansion and were imaged in negative ionization mode at a 10-µm acquisition resolution. Upon comparing the diameters of seminiferous tubules in both sets, an expansion factor of 4 was deduced, leading to an effective spatial resolution of 2.5 µm. Importantly, the architecture of the tubules remained unchanged post-expansion, validating the suitability of our method for tissues containing intricate tubular substructures.

Different species of seminolipids exhibited distinct localizations within the testis. Fig. 4a presents merged ion images of SGG (32:0), SGG (33:0), and PS (30:0), both with and without tissue expansion. The predominant species, SGG (33:0), was ubiquitously distributed throughout the tubules, while SGG (32:0) was primarily localized in the epithelial layer. Notably, tissue expansion enabled clearer visualization of the inner lumen. Additionally, a low-abundance lipid species, PS (30:0), was identified in the Leydig cells situated in the interstitial space, revealed through tissue expansion techniques. Fig. 4b illustrates a representative mass spectrum obtained from expanded mouse testicular tissue. Overall, we found 124 endogenous species, of which 78 were conclusively annotated as lipids, each with a mass error within the 5 ppm range. Suppl. Table 5 provides a comprehensive list of the detected lipid species.

Ex-MSI of lipids in mouse liver

To extend the applicability of our newly established Ex-MSI method, we applied it to mouse liver tissue. Slices of mouse liver were prepared both with and without tissue expansion and were subsequently imaged in negative ionization mode at a spatial resolution of 10 µm. By

measuring the diameters of hepatic blood vessels in both the expanded and non-expanded samples, we determined an expansion factor of 4.4, resulting in an effective spatial resolution of 2.3 µm. Fig. 4c displays ion images superimposed for phosphatidylethanolamine (PE) species PE (30:3;O3) and PE (36:2), lysophosphatidylinositol (LPI 18:0), and ceramide (Cer 40:2;O3), both in expanded (right) and non-expanded (left) states. The high resolution afforded by expansion allowed for intricate spatial elucidation of these lipid species. Fig. 4d provides a representative mass spectrum from expanded mouse liver tissue. In total, 181 endogenous molecular species were detected, of which 86 were assigned as lipids, all having a mass error within a 5 ppm threshold. The complete list of detected lipid species is enumerated in Suppl. Table 6. The liver's complex structure includes various cell types and intricate blood vessels. Reaching a 2.3 µm spatial resolution allows for detailed studies of these components, which could be valuable in understanding liver diseases and metabolic functions.

Conclusion

High-resolution lipid mass spectrometry imaging has been a focal point in biological research, but its growth has been hindered by limitations in achieving ultra-high spatial resolution. While MALDI-MSI techniques can reach subcellular dimensions, they impose stringent demands on sample preparation, matrix selection, and specialized ion sources, which may be barriers for many laboratories. Expansion-mass spectrometry imaging (Ex-MSI) presents a compelling alternative. Inspired by expansion microscopy methods initially designed for light microscopy, Ex-MSI provides a pathway to overcome the inherent spatial resolution limitations of conventional mass spectrometry instruments. It does so without requiring specialized ion sources or expensive labeling methods. As a result, Ex-MSI not only captures a comprehensive lipid profile in a single experiment but also significantly boosts the image resolution by 4.5 times to achieve near 1 μm spatial resolution. Additionally, it proves versatile in analyzing a diverse array of animal tissues with varied textures and substructures. Significantly, Ex-MSI offers a new methodological approach for the detailed study of cellular lipid metabolism, which may contribute to advancements in our current understanding of the field.

Acknowledgments: This study was supported by the General Research Fund (12302122) of the Research Grants Council, Hong Kong Special Administrative Region, China, the Start-up Grant from Hong Kong Baptist University, and the SKLEBA Research Grant (SKLP_2021_P04). We thank Dr. Jie Liu, Southern University of Science and Technology, for her help in fixation and staining experiments in expansion microscopy. We thank Dr. Paul Tillberg, Janelia Research Campus, HHMI, for the consultant and discussion on expansion microscopy. We thank Dr. Fei Chen, Broad Institute of MIT and Harvard, for the consultant on expansion microscopy experiments. We thank Dr. Lin Zhu and Dr. Zhu Yang, Hong Kong Baptist University, for the discussion of relevant academic issues.

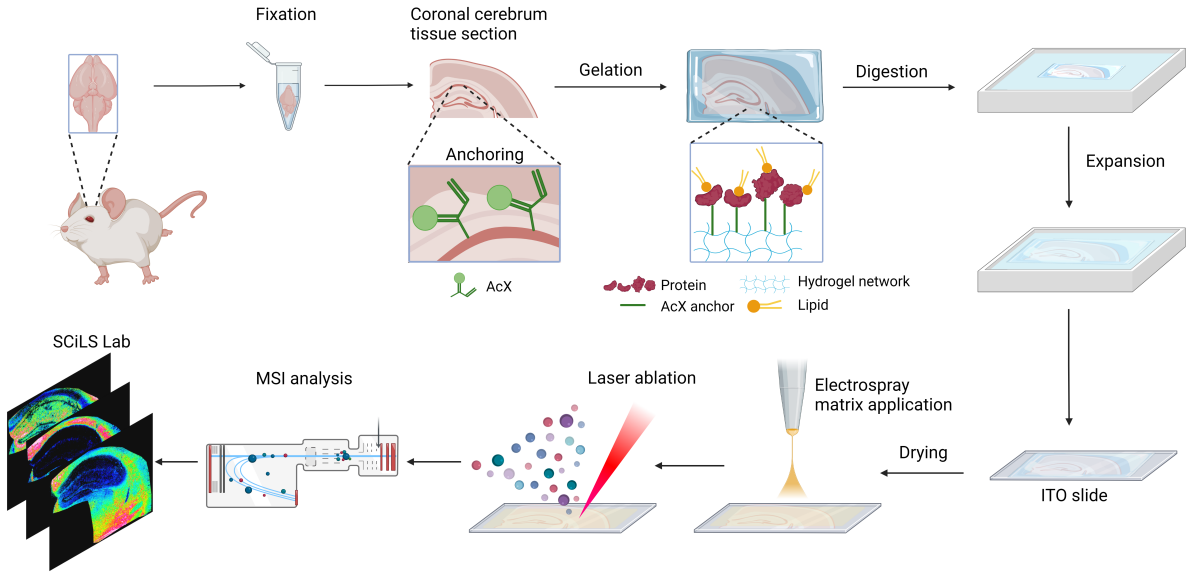

Fig. 1: Schematic Overview of Ex-MSI Workflow. This figure provides a step-by-step illustration of the experimental procedures involved in Ex-MSI (Expansion Mass Spectrometry Imaging), from sample preparation to data acquisition and analysis.

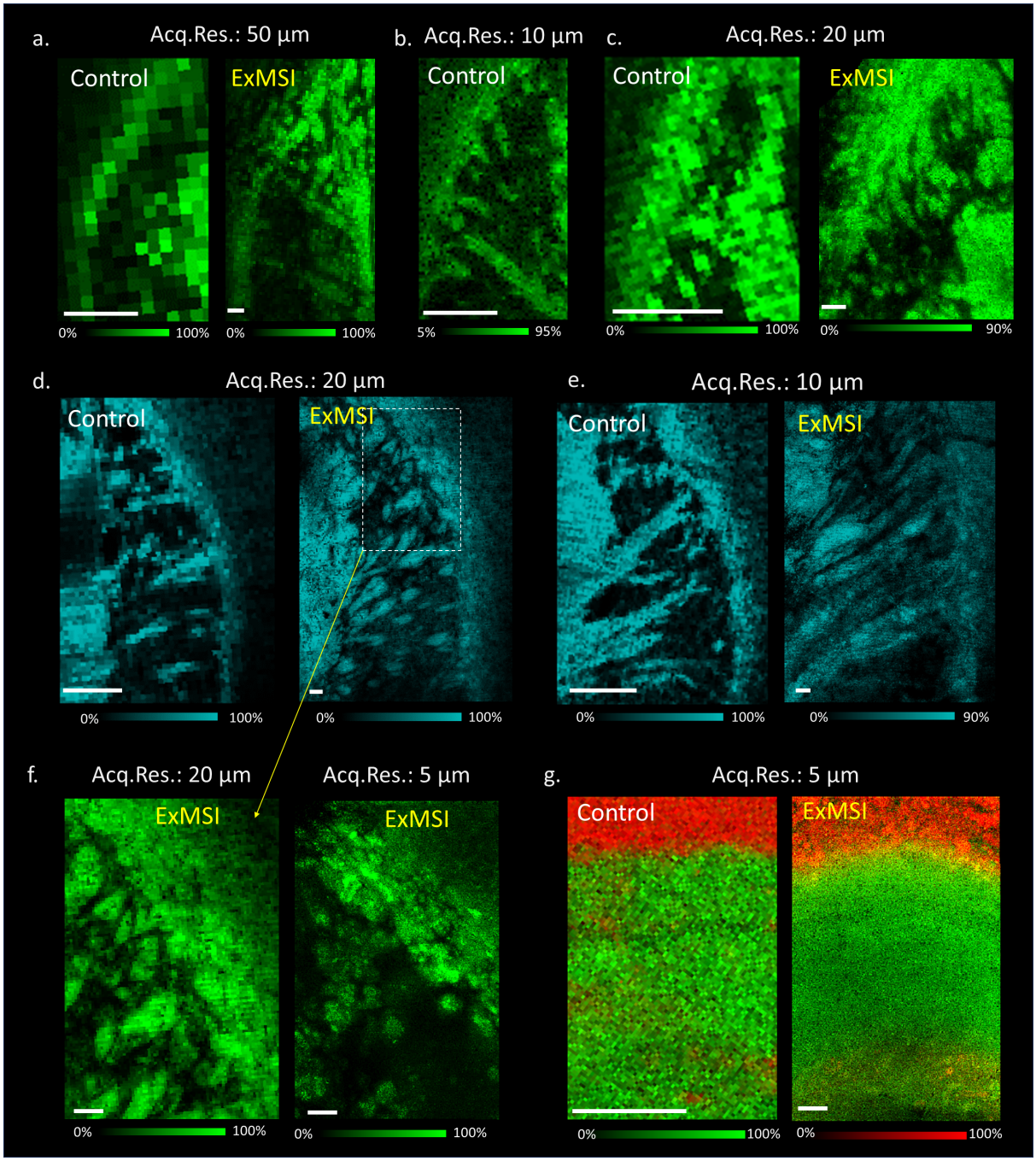

Fig. 2: Ex-MSI of mouse cerebrum tissue slices. (a, c) Positive mode ion images of m/z 850.8, PC-O (36:4) $[M+Na]^+$ in caudoputamen of the striatum region acquired with (a) 50 µm, and (c) 20 µm laser raster spot, respectively, resulting in an equivalent lateral spatial resolution of (a) 11 µm, and (c) 4.4 µm, respectively. (b) Positive mode ion image without expansion of the same ion in the same region acquired with 10 µm laser raster spot. (d-f) Negative mode ion images of m/z 888.6, SHexCer (42:2;O2) $[M-H]^-$ in caudoputamen of the striatum region

acquired with (d) 20 µm, (e) 10 µm, and (f) 5 µm laser raster spot, respectively, resulting in an equivalent lateral spatial resolution of (d) 4.4 µm, (e) 2.2 µm, and (f) 1.1 µm, respectively. (g) Negative mode ion images of m/z 888.6, SHexCer (42:2;O2) $[M-H]^-$ (red), and m/z 718.5, PE (34:0) $[M-H]^-$ (green) in alv and CA1 of the hippocampus region acquired with 5 µm laser raster spot, respectively, resulting in an equivalent lateral spatial resolution of 1.1 µm. In (a, c, d, e, g), the left and right panel displays the ion images without and with expansion, respectively. The acquisition resolution (Acq. Res) is from 50 to 10 µm, which was equivalent to image equivalent resolution (Eq. Res) of 11 to 2.2 µm. Scale bar represents 200 µm.

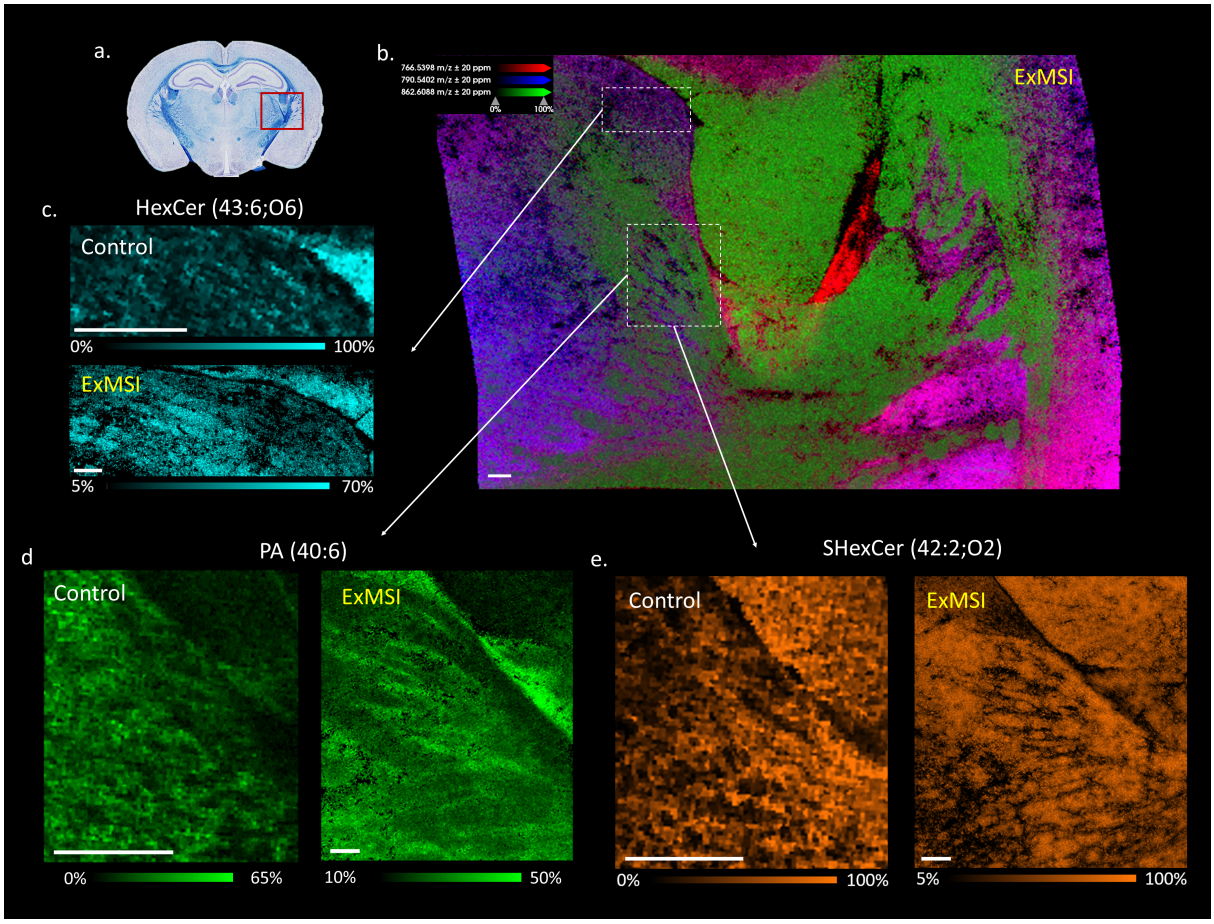

Fig. 3: High-resolution lipid mapping in mouse brain cerebrum via Ex-MSI. Negative ion mode images were acquired using a 10 µm laser raster spot, yielding an equivalent spatial resolution of 2.2 µm. (a) Coronal section of a mouse brain. Image courtesy from Bmonzon, Wikipedia, licensed under CC BY-SA 4.0. The red frame indicated the imaging area of (b). (b) Overlaid ion image of PE (38:4) ($[M-H]^-$, m/z 766.5), PE (40:6) ($[M-H]^-$, m/z 790.5), and SHexCer (40:1;O2) ($[M-H]^-$, m/z 862.6). Panels (c-e) offer side-by-side comparisons between non-expanded and expanded ion images. (c) The fibrous structure of the dorsal part in the lateral geniculate complex could be observed with the ion images of HexCer (43:6;O6) ($[M-H]^-$, m/z 878.6). (d, e) In the ventral posteromedial nucleus region of the thalamus, distribution of PA (40:6) ($[M-H]^-$, m/z 747.5) and SHexCer (42:2;O2) ($[M-H]^-$, m/z 888.6) were shown. Scale bar represents 300 µm.

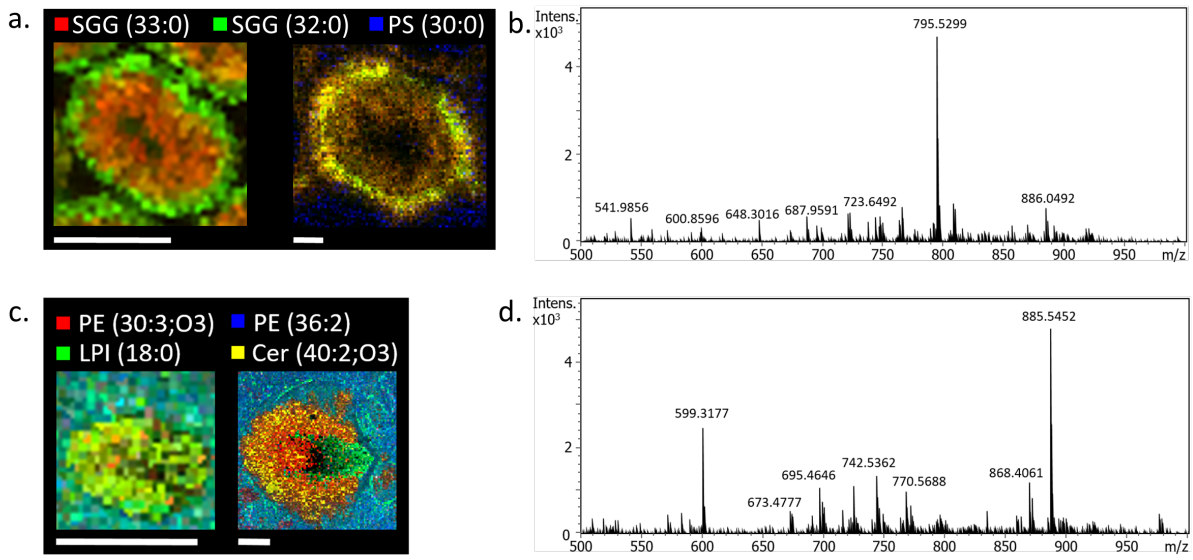

Fig. 4: Ex-MSI in mouse testis and liver tissues. The left and right panel displays the ion images without and with expansion, respectively. (a) The overlaid distribution of SSG (33:0) ([M-H]$^-$, m/z 809.5), SSG (32:0) ([M-H]$^-$, m/z 795.5) and PS (30:0) ([M+Cl]$^-$, m/z 742.4) in testis. Imaging was conducted in negative mode, using a 10 µm laser raster spot, yielding an equivalent lateral spatial resolution of 2.5 µm. (b)Representative mass spectrum obtained from expanded mouse testicular tissue. (c)The overlaid distribution of PE (30:3;O3) ([M-H]$^-$, m/z 704.4), PE (36:2) ([M-H]$^-$, m/z 742.5), LPI (18:0) ([M-H]$^-$, m/z 599.3), and Cer (40:2;O3) ([M-H]$^-$, m/z 634.6) in liver. Imaging was conducted in negative mode, using a 10 µm laser raster spot, yielding an equivalent lateral spatial resolution of 2.3 µm. (d) Representative mass spectrum obtained from expanded mouse liver tissue. Scale bar represents 100 µm.

References

[1] C. Werner, M. Sauer, C. Geis, Super-resolving Microscopy in Neuroscience, Chem Rev, 121 (2021) 11971-12015.
[2] P. Padmanabhan, A. Kneynsberg, J. Gotz, Super-resolution microscopy: a closer look at synaptic dysfunction in Alzheimer disease, Nat Rev Neurosci, 22 (2021) 723-740.
[3] R.E. Leighton, A.M. Alperstein, R.R. Frontiera, Label-Free Super-Resolution Imaging Techniques, Annu Rev Anal Chem (Palo Alto Calif), 15 (2022) 37-55.
[4] D. Choquet, M. Sainlos, J.B. Sibarita, Advanced imaging and labelling methods to decipher brain cell organization and function, Nat Rev Neurosci, 22 (2021) 237-255.
[5] S.C. Bendall, E.F. Simonds, P. Qiu, A.D. Amir el, P.O. Krutzik, R. Finck, R.V. Bruggner, R. Melamed, A. Trejo, O.I. Ornatsky, R.S. Balderas, S.K. Plevritis, K. Sachs, D. Pe'er, S.D. Tanner, G.P. Nolan, Single-cell mass cytometry of differential immune and drug responses across a human hematopoietic continuum, Science, 332 (2011) 687-696.
[6] J.W. Hickey, E.K. Neumann, A.J. Radtke, J.M. Camarillo, R.T. Beuschel, A. Albanese, E. McDonough, J. Hatler, A.E. Wiblin, J. Fisher, J. Croteau, E.C. Small, A. Sood, R.M. Caprioli, R.M. Angelo, G.P. Nolan, K. Chung, S.M. Hewitt, R.N. Germain, J.M. Spraggins, E. Lundberg, M.P. Snyder, N.L. Kelleher, S.K. Saka, Spatial mapping of protein composition and tissue organization: a primer for multiplexed antibody-based imaging, Nat Methods, 19 (2022) 284-295.
[7] K. Chughtai, R.M. Heeren, Mass spectrometric imaging for biomedical tissue analysis, Chem Rev, 110 (2010) 3237-3277.
[8] J.L. Norris, R.M. Caprioli, Analysis of tissue specimens by matrix-assisted laser desorption/ionization imaging mass spectrometry in biological and clinical research, Chem Rev, 113 (2013) 2309-2342.
[9] K.A. Berry, J.A. Hankin, R.M. Barkley, J.M. Spraggins, R.M. Caprioli, R.C. Murphy, MALDI imaging of lipid biochemistry in tissues by mass spectrometry, Chem Rev, 111 (2011) 6491-6512.
[10] I.S. Gilmore, S. Heiles, C.L. Pieterse, Metabolic Imaging at the Single-Cell Scale: Recent Advances in Mass Spectrometry Imaging, Annu Rev Anal Chem (Palo Alto Calif), 12 (2019) 201-224.
[11] L. Keren, M. Bosse, S. Thompson, T. Risom, K. Vijayaragavan, E. McCaffrey, D. Marquez, R. Angoshtari, N.F. Greenwald, H. Fienberg, J. Wang, N. Kambham, D. Kirkwood, G. Nolan, T.J. Montine, S.J. Galli, R. West, S.C. Bendall, M. Angelo, MIBI-TOF: A multiplexed imaging platform relates cellular phenotypes and tissue structure, Sci Adv, 5 (2019) eaax5851.
[12] M. Angelo, S.C. Bendall, R. Finck, M.B. Hale, C. Hitzman, A.D. Borowsky, R.M. Levenson, J.B. Lowe, S.D. Liu, S. Zhao, Y. Natkunam, G.P. Nolan, Multiplexed ion beam imaging of human breast tumors, Nat Med, 20 (2014) 436-442.
[13] C. Giesen, H.A. Wang, D. Schapiro, N. Zivanovic, A. Jacobs, B. Hattendorf, P.J. Schuffler, D. Grolimund, J.M. Buhmann, S. Brandt, Z. Varga, P.J. Wild, D. Gunther, B. Bodenmiller, Highly multiplexed imaging of tumor tissues with subcellular resolution by mass cytometry, Nat Methods, 11 (2014) 417-422.
[14] M.H. Spitzer, G.P. Nolan, Mass Cytometry: Single Cells, Many Features, Cell, 165 (2016) 780-791.
[15] Y. Bai, B. Zhu, J.P. Oliveria, B.J. Cannon, D. Feyaerts, M. Bosse, K. Vijayaragavan, N.F. Greenwald, D. Phillips, C.M. Schurch, S.M. Naik, E.A. Ganio, B. Gaudilliere, S.J. Rodig, M.B. Miller, M. Angelo, S.C. Bendall, X. Rovira-Clave, G.P. Nolan, S. Jiang, Expanded vacuum-stable gels for multiplexed high-resolution spatial histopathology, Nat Commun, 14 (2023) 4013.
[16] M. Kompauer, S. Heiles, B. Spengler, Atmospheric pressure MALDI mass spectrometry imaging of tissues and cells at 1.4-µm lateral resolution, Nature Methods, 14 (2017) 90-96.
[17] D.C. Castro, Y.R. Xie, S.S. Rubakhin, E.V. Romanova, J.V. Sweedler, Image-guided MALDI mass spectrometry for high-throughput single-organelle characterization, Nature Methods, 18 (2021) 1233-1238.

[18] M. Niehaus, J. Soltwisch, M.E. Belov, K. Dreisewerd, Transmission-mode MALDI-2 mass spectrometry imaging of cells and tissues at subcellular resolution, Nature Methods, 16 (2019) 925-931.
[19] L. Capolupo, I. Khven, A.R. Lederer, L. Mazzeo, G. Glousker, S. Ho, F. Russo, J.P. Montoya, D.R. Bhandari, A.P. Bowman, S.R. Ellis, R. Guiet, O. Burri, J. Detzner, J. Muthing, K. Homicsko, F. Kuonen, M. Gilliet, B. Spengler, R.M.A. Heeren, G.P. Dotto, G.L. Manno, G. D'Angelo, Sphingolipids control dermal fibroblast heterogeneity, Science, 376 (2022) eabh1623.
[20] E. Cuypers, B.S.R. Claes, R. Biemans, N.G. Lieuwes, K. Glunde, L. Dubois, R.M.A. Heeren, 'On the Spot' Digital Pathology of Breast Cancer Based on Single-Cell Mass Spectrometry Imaging, Analytical Chemistry, 94 (2022) 6180-6190.
[21] B. Geier, E.M. Sogin, D. Michellod, M. Janda, M. Kompauer, B. Spengler, N. Dubilier, M. Liebeke, Spatial metabolomics of in situ host–microbe interactions at the micrometre scale, Nat Microbiol, 5 (2020) 498-510.
[22] G. Wang, B. Heijs, S. Kostidis, A. Mahfouz, R.G.J. Rietjens, R. Bijkerk, A. Koudijs, L.A.K.v.d. Pluijm, C.W.v.d. Berg, S.J. Dumas, P. Carmeliet, M. Giera, B.M.v.d. Berg, T.J. Rabelink, Analyzing cell-type-specific dynamics of metabolism in kidney repair, Nat Metabolism, 4 (2022) 1109-1118.
[23] G. Wang, B. Heijs, S. Kostidis, R.G.J. Rietjens, M. Koning, L. Yuan, G.L. Tiemeier, A. Mahfouz, S.J. Dumas, M. Giera, J. Kers, S.M.C.d.S. Lopes, C.W.v.d. Berg, B.M.v.d. Berg, T.J. Rabelink, Spatial dynamic metabolomics identifies metabolic cell fate trajectories in human kidney differentiation, Cell Stem Cell, 29 (2022) 1580-1593.e1587.
[24] A.A. Nikitina, A.V. Grouw, T. Roysam, D. Huang, F.M. Fernández, M.L. Kemp, Mass Spectrometry Imaging Reveals Early Metabolic Priming of Cell Lineage in Differentiating Human-Induced Pluripotent Stem Cells, Analytical Chemistry, 95 (2023) 4880-4888.
[25] M.A. Müller, N. Zweig, B. Spengler, M. Weinert, S. Heiles, Lipid Signatures and Inter-Cellular Heterogeneity of Naïve and Lipopolysaccharide-Stimulated Human Microglia-like Cells, Analytical Chemistry, 95 (2023) 11672-11679.
[26] S. Bessler, J. Soltwisch, K. Dreisewerd, Visualization of Differential Cardiolipin Profiles in Murine Retinal Cell Layers by High-Resolution MALDI Mass Spectrometry Imaging, Analytical Chemistry, 95 (2023) 11352-11358.
[27] H. Zhang, Y. Liu, L. Fields, X. Shi, P. Huang, H. Lu, A.J. Schneider, X. Tang, L. Puglielli, N.V. Welham, L. Li, Single-cell lipidomics enabled by dual-polarity ionization and ion mobility-mass spectrometry imaging, Nat. Commun., 14 (2023) 5185.
[28] B.M. White, P. Kumar, A.N. Conwell, K. Wu, J.M. Baskin, Lipid Expansion Microscopy, J Am Chem Soc, 144 (2022) 18212-18217.
[29] D.-e. Sun, X. Fan, Y. Shi, H. Zhang, Z. Huang, B. Cheng, Q. Tang, W. Li, Y. Zhu, J. Bai, W. Liu, Y. Li, X. Wang, X. Lei, X. Chen, Click-ExM enables expansion microscopy for all biomolecules, Nature Methods, 18 (2021) 107-113.
[30] J. Park, S. Khan, D.H. Yun, T. Ku, K.L. Villa, J.E. Lee, Q. Zhang, J. Park, G. Feng, E. Nedivi, K. Chung, Epitope-preserving magnified analysis of proteome (eMAP), Science Advances, 7 (2021) eabf6589.
[31] A. Klimas, B.R. Gallagher, P. Wijesekara, S. Fekir, E.F. DiBernardo, Z. Cheng, D.B. Stolz, F. Cambi, S.C. Watkins, S.L. Brody, A. Horani, A.L. Barth, C.I. Moore, X. Ren, Y. Zhao, Magnify is a universal molecular anchoring strategy for expansion microscopy, Nat Biotechnol, (2023) 1-12.
[32] H.G.J. Damstra, B. Mohar, M. Eddison, A. Akhmanova, L.C. Kapitein, P.W. Tillberg, Visualizing cellular and tissue ultrastructure using Ten-fold Robust Expansion Microscopy (TREx), Elife, 11 (2022) e73775.
[33] A.T. Wassie, Y. Zhao, E.S. Boyden, Expansion microscopy: principles and uses in biological research, Nature Methods, 16 (2019) 33-41.
[34] E.D. Karagiannis, J.S. Kang, T.W. Shin, A. Emenari, S. Asano, L. Lin, E.K. Costa, I.G.C. Consortium, A.H. Marblestone, N. Kasthuri, E.S. Boyden, Expansion Microscopy of Lipid Membranes, bioRxiv, (2019) 829903.

[35] S. Truckenbrodt, M. Maidorn, D. Crzan, H. Wildhagen, S. Kabatas, S.O. Rizzoli, X10 expansion microscopy enables 25-nm resolution on conventional microscopes, Embo Rep, 19 (2018) e45836.
[36] T.J. Chozinski, A.R. Halpern, H. Okawa, H.-J. Kim, G.J. Tremel, R.O.L. Wong, J.C. Vaughan, Expansion microscopy with conventional antibodies and fluorescent proteins, Nature Methods, 13 (2016) 485-488.
[37] T. Ku, J. Swaney, J.-Y. Park, A. Albanese, E. Murray, J.H. Cho, Y.-G. Park, V. Mangena, J. Chen, K. Chung, Multiplexed and scalable super-resolution imaging of three-dimensional protein localization in size-adjustable tissues, Nat Biotechnol, 34 (2016) 973-981.
[38] P.W. Tillberg, F. Chen, K.D. Piatkevich, Y. Zhao, C.-C. Yu, B.P. English, L. Gao, A. Martorell, H.-J. Suk, F. Yoshida, E.M. DeGennaro, D.H. Roossien, G. Gong, U. Seneviratne, S.R. Tannenbaum, R. Desimone, D. Cai, E.S. Boyden, Protein-retention expansion microscopy of cells and tissues labeled using standard fluorescent proteins and antibodies, Nat Biotechnol, 34 (2016) 987-992.
[39] F. Chen, P.W. Tillberg, E.S. Boyden, Expansion microscopy, Science, 347 (2015) 543-548.
[40] C. Villette, L. Maurer, J. Zumsteg, J. Mutterer, A. Wanko, D. Heintz, Mass spectrometry imaging for biosolids characterization to assess ecological or health risks before reuse, Nat. Commun., 14 (2023) 4244.
[41] L. Wang, X. Xing, X. Zeng, S.R. Jackson, T. TeSlaa, O. Al-Dalahmah, L.Z. Samarah, K. Goodwin, L. Yang, M.R. McReynolds, X. Li, J.J. Wolff, J.D. Rabinowitz, S.M. Davidson, Spatially resolved isotope tracing reveals tissue metabolic activity, Nature Methods, 19 (2022) 223-230.
[42] M. Schwaiger-Haber, E. Stancliffe, D.S. Anbukumar, B. Sells, J. Yi, K. Cho, K. Adkins-Travis, M.G. Chheda, L.P. Shriver, G.J. Patti, Using mass spectrometry imaging to map fluxes quantitatively in the tumor ecosystem, Nat. Commun., 14 (2023) 2876.
[43] J. Leopold, P. Prabutzki, K.M. Engel, J. Schiller, A Five-Year Update on Matrix Compounds for MALDI-MS Analysis of Lipids, Biomolecules, 13 (2023).
[44] J. Wang, S. Qiu, S. Chen, C. Xiong, H. Liu, J. Wang, N. Zhang, J. Hou, Q. He, Z. Nie, MALDI-TOF MS imaging of metabolites with a N-(1-naphthyl) ethylenediamine dihydrochloride matrix and its application to colorectal cancer liver metastasis, Anal Chem, 87 (2015) 422-430.
[45] H. Liu, R. Chen, J. Wang, S. Chen, C. Xiong, J. Wang, J. Hou, Q. He, N. Zhang, Z. Nie, L. Mao, 1,5-Diaminonaphthalene hydrochloride assisted laser desorption/ionization mass spectrometry imaging of small molecules in tissues following focal cerebral ischemia, Anal Chem, 86 (2014) 10114-10121.
[46] A.R. Korte, Y.J. Lee, MALDI-MS analysis and imaging of small molecule metabolites with 1,5-diaminonaphthalene (DAN), J Mass Spectrom, 49 (2014) 737-741.
[47] C.D. Cerruti, F. Benabdellah, O. Laprevote, D. Touboul, A. Brunelle, MALDI imaging and structural analysis of rat brain lipid negative ions with 9-aminoacridine matrix, Anal Chem, 84 (2012) 2164-2171.